Universidad de Concepción

Facultad de Ciencias Físicas y Matemáticas

Magíster en Ciencias mención en Física

# Towards a possible formation scenario for dwarf spheroidal galaxies with angular momentum

(En camino a un posible escenario de formación de galaxias enanas esferoidales con momento angular)

Tesis para optar al grado Magíster en Ciencias mención Física

**Jocelyn Nicole Hazeldine Lefenda**

Profesor Guía:

Dr. Michael Fellhauer

Facultad de Ciencias Físicas y Matemáticas

Universidad de Concepción

Chile

Concepción, August 17, 2018

UNIVERSIDAD DE CONCEPCIÓN

# Resumen

Facultad de Ciencias Físicas y Matemáticas

Departamento de Astronomía

## En camino a un posible escenario de formación de galaxias enanas con momentum angular

por Jocelyn Hazeldine

Las galaxias enanas esferoidales (dSph) son consideradas como los ladrillos en la formación de galaxias y se cree además que son los sistemas más dominados de materia oscura que se conocen. Existen varios modelos que intentan explicar su formación, pero estos tienen problemas al modelar la formación de estas galaxias en aislamiento. Aquí, mostramos un posible escenario de formación donde cúmulos de estrellas son formados en un halo de materia oscura de una dSph. Estos cúmulos de estrellas tienen baja eficiencia de formación estelar y se estan disolviendo mientras orbitan el halo, formando así la débil componente luminosa que observamos. En este proyecto estudiamos una extensión de este escenario incluyendo el momento angular a nuestra distribución de cúmulos de estrellas. Nuestro objetivo es descubrir si hay una región de transición definida entre galaxias dSph y galaxias enanas de disco dominadas por rotación.

UNIVERSIDAD DE CONCEPCIÓN

# *Abstract*

Facultad de Ciencias Físicas y Matemáticas

Departamento de Astronomía

Magíster en Ciencias mención Física

**Towards a possible formation scenario for dwarf spheroidal galaxies with angular momentum**

by Jocelyn Hazeldine

Dwarf spheroidal (dSph) galaxies are considered the building blocks of galaxy formation and they are believed to be the most dark matter dominated systems known. There are several models that attempt to explain their formation, but they have problems to model the formation of these galaxies in isolation. Here, we show a possible formation scenario in which star clusters (SC) are forming in a dark matter halo of a dSph. These SCs have low star formation efficiencies and they are dissolving while orbiting the halo, forming the faint luminous component that we observe. In this project we study an extension of this scenario by including angular momentum into our SC distribution. Our goal is to find out if there is a defined transition region between dSph and dwarf disc galaxies driven by rotation.

# Contents

# List of Tables

# List of Figures

# Chapter 1

# Introduction

## 1.1 Dwarf spheroidal galaxies

The Local Group (LG) is an assembly of galaxies which are gravitationally bound and where our galaxy, the Milky Way (MW) belongs to. This group is formed by three major galaxies (MW, Andromeda and Triangulum) and the rest of the members are satellites of these three galaxies or isolated dwarfs orbiting the gravitational center. About a hundred members have been recognized and the most common ones are the dwarf spheroidal (dSph) galaxies (McConnachie, 2012).

The dSph galaxies are the smallest galactic systems known (Battaglia et al., 2013). With sizes of a few hundred parsecs (McConnachie, 2012) this kind of galaxies are characterized by having the lowest surface brightness ($\mu_{0,V} \sim 22.5 - 27$ mag/arcsec$^2$) and by being the faintest galaxies known (M$_V$ -13 to -9) (Battaglia et al., 2013). They almost do not have interstellar gas implying no active star formation. Also, they show low rotation velocities (Grebel et al., 2003) and are dominated by dispersion with velocities around $\sim 10$ km/s (Walker et al., 2007). One of their main features is the high content of dark matter (DM). They are in fact the most DM-dominated systems in the Universe (Battaglia et al., 2013), showing mass-to-light ratios of hundred or even larger. All this characteristics are summarized in Table 1.1.

| Characteristic | Value |
|---|---|
| Half light radii $r$ | 0.1 - 0.5 kpc |
| Absolute magnitude $M_V$ | $-9$ to $-13$ mag |
| Central Surface brightness $\mu_{0,v}$ | $22.5 - 27$ mag/arsec$^2$ |
| Velocity dispersion $\sigma$ | $5 - 12$ km/s |
| Total Mass $M$ | $10^7 - 10^8 M_\odot$ |
| Mass-to-Light ratio (M/L) | $\sim 10 - 300$ |

TABLE 1.1: Dwarf spheroidal galaxies main characteristics (excluding faint and ultrafaint dwarf galaxies), based on different authors (Mateo (1998), Grebel et al. (2003), Walker et al. (2007),Lokas (2011),McConnachie (2012) and Battaglia et al. (2013)) Table prepared by the author based on the mentioned authors.

In the Lambda Cold Dark Matter ($\Lambda$CDM) cosmology, the formation of galaxies is hierarchical, meaning, at the beginning, small DM haloes are formed and then they give way to form other structures, larger and complex ones (White & Rees, 1978). Considering this, dSph galaxies are believed to be the building blocks or seeds in galaxy formation (Kauffmann et al., 1993) and they have a big importance constraining galaxy formation theories. Comparing cosmological simulations with observations a problem showed up. A mismatch between the number of predicted subhaloes and the number of observed ones is known as the missing satellite problem (Klypin et al., 1999) which is now close to being solved. In the last few years, with the increasing number of dSph galaxies that have been found by surveys such as the Sloan Digital Sky Survey (SDSS) (York et al., 2000) and the discovery of the ultrafaint galaxies this mismatch is now smaller and smaller, and the problem is expected to be solved in the near future with new observations.

The Universe energy density is composed by an approximately 26% of DM (Planck Collaboration et al., 2016). Actually, there is no explanation what DM is, but there are some candidates, for example, weakly interacting massive particles (WIMPs), neutrinos, axions and others. (Feng, 2010).

As we mentioned before, dSph galaxies are characterized to show high mass-to-light (M/L) ratios which means that these objects have more mass than luminous content implying a large amount of DM, they are dominated by it (Mateo (1998), McConnachie (2012)). In order to study and constrain DM theories, dSph galaxies are the most attractive object for DM searches (Porter et al., 2011) for example, in the search of gamma

rays produced by DM annihilations or decay (Abdo et al., 2010).

So far we have talked about what we know about dSph galaxies and why they are important, but in order to understand dSph galaxies we also need to know where these galaxies are coming from and how they have been formed.

## 1.2 Formation theories of dSph galaxies

In general, the formation of dSph galaxies is not completely clear, but some models exist which try to explain it. These models are divided into two categories, the first one are models which consider an interaction between galaxies as a mechanism to form a dSph galaxy and the second category considers the formation of these objects in isolation as a result of their own evolution. However, we can mention that all models which consider some kind of interaction are not using the fact that these galaxies are considered to be the building blocks in galaxy formation.

In this section I will discuss some examples of dSph formation models of both cases: with and without galaxies interaction:

### 1.2.1 The tidal stirring and ram pressure model

In a paper published by Mayer et al. (2007), they explain a method to form dSph galaxies as the result of an interaction between a rotationally supported dwarf disc galaxy and a larger system (MW-sized). Tidal shocks and ram pressure are responsible to remove the gas from the dwarf. This gas is already loosely bound because of the participation of the cosmic ultraviolet (UV) background which heats and ionizes the gas while the dwarf galaxy is falling into the host galaxy potential well. At the end, when the gas is removed there is only a tiny stellar content remaining which corresponds to a dSph galaxy.

To perform this project, they use a high resolution N-body and smoothed particle hydrodynamics (SPH) model of a dwarf galaxy which has a disk of stars and gas within a cold dark matter halo. In this context, they assume that 80% of the baryonic component is gas.

The dwarfs in this model are considered satellites of the larger system in eccentric orbits with orbital times of about 1.7 Gyr. At the first passage the dwarf dark halo loses 60% of its initial mass and as two orbits are completed there is no gas in the dwarf left. The gas

is taken away by tides and ram pressure when the dwarf approached the pericenter, removing the outer disk. This happens because the ram pressure force is stronger than the gravitational restoring force of the dark halo. At the second pericenter an instantaneous ram pressure stripping occurs because the density of the halo is decreased and then the gravitational restoring force too, also due to tidal shocks the dwarf loses gas until one initial disk scale length approximately. On the last orbits the stellar velocity dispersion is flat in agreement with observed galaxies like Draco and Ursa Minor. And an important part of the halo is kept on few kiloparsecs from the center obtaining $M/L$ larger than 100.

With their work they affirm that all massive galaxies should have DM-dominated satellites. But they recognize the presence of isolated dSph galaxies such as Tucana is a challenge for their model, considering their location far away from any massive galaxy.

### 1.2.2   The resonant stripping model

The authors who proposed this model (D'Onghia et al., 2009) performed simulations of encounters between dwarf disc galaxies and they found that the process which transforms them into a dSph galaxy is resonant stripping. This process is different from the one described above, because it is driven by gravitational resonances.

To develop this model they run numerical simulations to study the consequences of dwarf galaxies encounters. The process which removes the stars of the smaller galaxy is a resonance between the spin angular frequency of its disk and the angular frequency of its orbit around the larger galaxy. In a prograde encounter, when these frequencies are comparable in magnitude and the spin and orbital angular momenta are somewhat aligned, the gravitational perturbation from the larger dwarf on a patch of the smaller disk is always directed outwards from its center, leading to significant stripping. The resonant stripping process is most effective during an interaction with prograde orbits obtaining at the end surface mass profiles and kinematic properties similar to those we can observe in the LG spheroidals. A representation of what happens in prograde and retrograde orbits is shows in Figure 1.1.
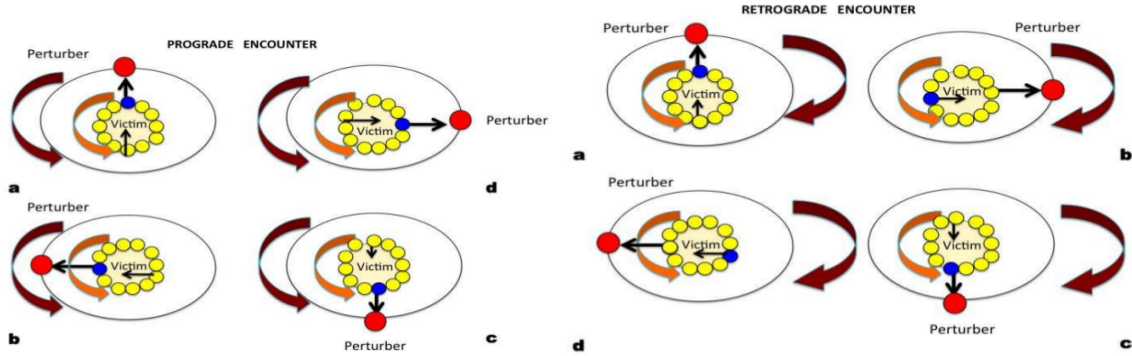
FIGURE 1.1: This scheme explains the behavior of prograde (left plot) and retrograde (right plot) scenarios. The victim correspond to the small dwarf galaxy and the perturber to the larger dwarf, circles are the star particles of the victim and they are rotating in the disk. In the prograde case, following the blue circle we can see that this particles are pulled inward or outward depending of their position respect to the gravitational perturbation of the perturber. In the other case, the stars in the disk are pulled inward and outward alternately. Credit to D'Onghia et al. (2009)

The time evolution of an encounter between two dwarf disc galaxies is shown in the first row of Figure 1.2. The bigger one is 100 times bigger than the smaller one. After two billions years $\sim 80\%$ of the stars are lost from the smaller galaxy but the dark halo is almost not affected. The interacting dwarfs were chosen to have similar characteristics to the ones in the LG. The authors also mention that they could get ultrafaint dwarf galaxies if they choose suitable initial conditions. (D'Onghia et al., 2009)

### 1.2.3 Formation of isolated dwarf galaxies with feedback

Sawala et al. (2010) model the formation and evolution of dwarf galaxies using high-resolution hydrodynamical simulations including cooling, star formation, feedback from type II and Ia supernovae and UV background radiation. Unlike with the previous models where dSph simulations were run, in this case they work with big cosmological $\Lambda$CDM simulations with zoom-in to barely resolve the dSph regime. In their model, gas particles were converted into star particles if the density is sufficiently high but they did not consider that stars are formed in clusters or associations (Lada & Lada, 2003) because it is below their resolution.

As a result of their project, they obtain galaxies with similar characteristics as the larger LG dwarf spheroidals which are the product of a combination of feedback and the cosmic UV background. Also they found two types of age distribution with analogous to the LG, a single burst of 1 Gyr and a burst with a tail which is extending up to several Gyr. However, they can not reproduce galaxies with characteristics like the Fornax galaxy (luminosity and shape) nor obtain ultrafaint galaxies.
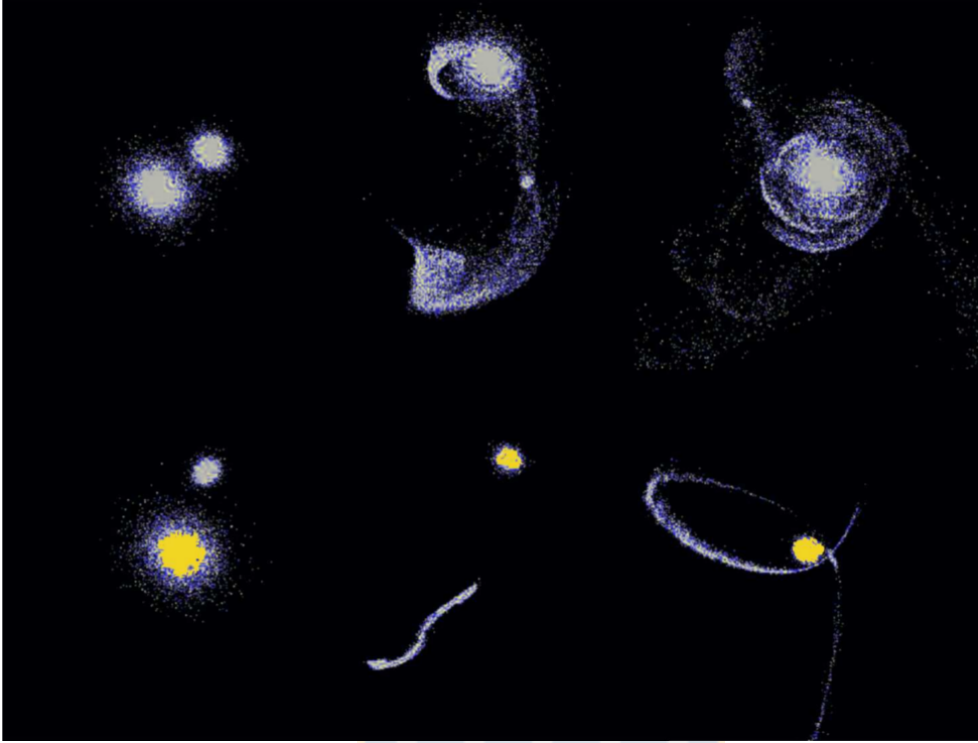
FIGURE 1.2: In the top row we have a interaction of the stellar content between two dwarf disc galaxies, the larger one is 100 times larger than the smaller one. The left panel shows up the initial set up with the galaxies interact in prograde orbits. The next panel is obtain after 2 billion years after the first pericenter and finally the right panel shows the interaction after 7 billion years. The bottom row show a different case if the larger galaxy is the MW (ten thousands bigger than the smaller one) and the interaction is show in the same way, 2 and finally 7 billion years. Credit to D'Onghia et al. (2009)

### 1.2.4 Dissolving star clusters model

This model, as the one explained just before, does not consider an interaction with other galaxies. It was proposed by Assmann et al. (2013a) and basically, this model says that a dSph galaxy can be formed after the dissolution of several star clusters (SCs) due to gas expulsion which will form the luminous component of the dwarf within a DM halo. This model is based on the $\Lambda$CDM hierarchical formation and the fact that stars always form in clusters or associations (Lada & Lada, 2003). In this scenario they place several SCs in a DM halo which are set with low star formation efficiency (SFE) so, they are destinated to dissolve. While orbiting the central part of the DM halo the dissolving SCs spread their stars and build up the luminous component of the dSph satellites we see today. Using this model they can explain dSph galaxies in isolation, their kinematics and morphologies.

As a result, they obtain final objects with similar properties to the classical dSph galaxies. They found velocity dispersion is in a range of $5-10$ km/s (in agreement with the

information in Table 1.1) and as we can see in Figure 1.3, this velocity stays flat and does not fall at large radii which is an indicator that the object is dominated by DM. Also, in the dispersion profiles some bumps can be visualized and these can not be associated to errors. These characteristics also appear in observations, but in these cases, as the data points have larger error bars, they go unnoticed. However, as the bumps also appeared in this model they believe that these are real characteristics.
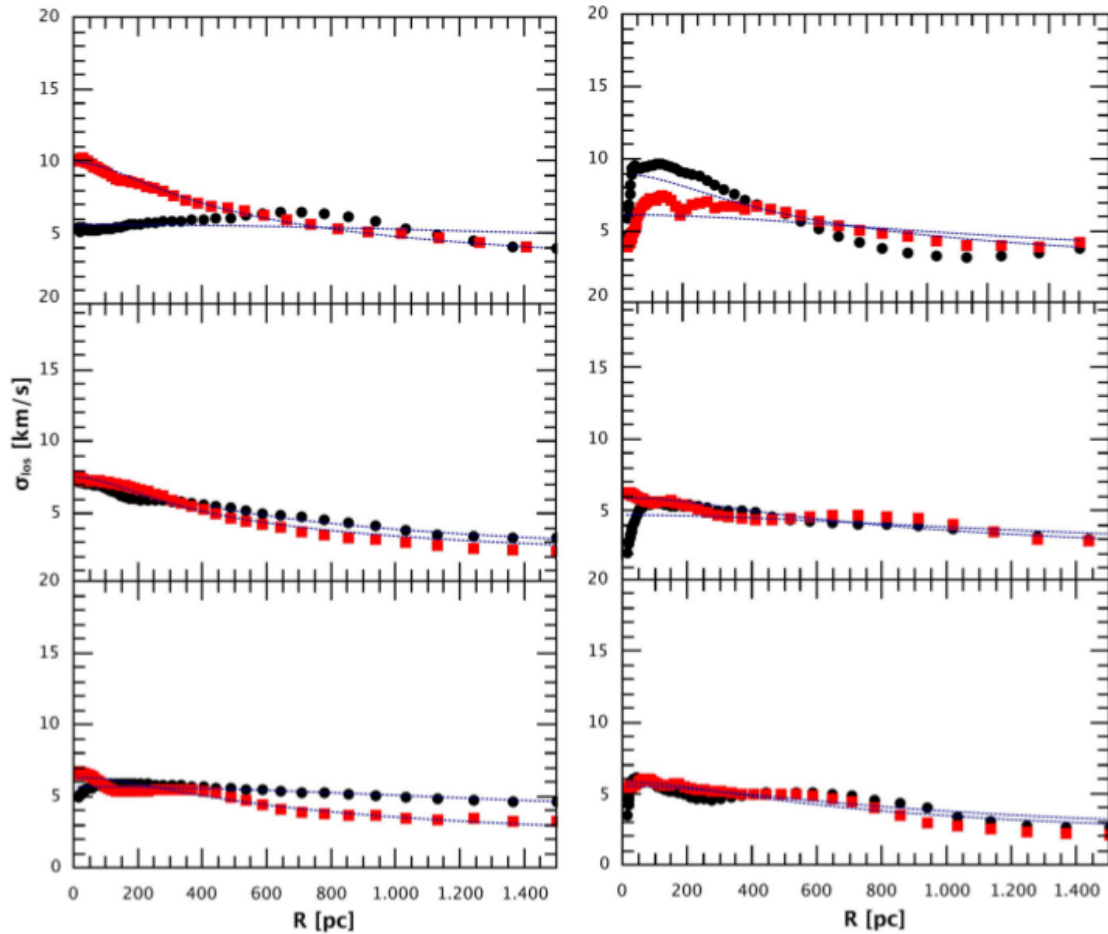


FIGURE 1.3: Line-of-sight velocity dispersion for cusped and cored DM haloes (left and right respectively). In the top panels the scale-lengths of the DM halo is 1.0, in the middle panels is 0.5 and at the bottom 0.25 kpc. The color red indicate that initially are 15 SCs and black correspond to 30 SCs. Finally, in both cases a more or less flat profile is obtain. Credit to Assmann et al. (2013b)

The left and middle panels of 1.4 show the surface brightness maps from one final object from this scenario in 100 pc and 25 pc of resolution (top and bottom respectively). From the left panels we can mention that they obtain an object which is in agreement with a dSph galaxy because it has a magnitude in a range of 28.2 and 33.5 per arsec$^2$ (see Table 1.1) also, in the middle panel they make a restriction using the telescope limit from Majewski et al. (2005) and give us an idea of what a telescope can observe subtracting

all the diffuse parts from the dwarf. Finally in the right panels we can find contours of the model using a resolution of 50 pc pixel$^{-1}$, the top panel correspond to a logarithmic scale and the bottom one has a linear scale.
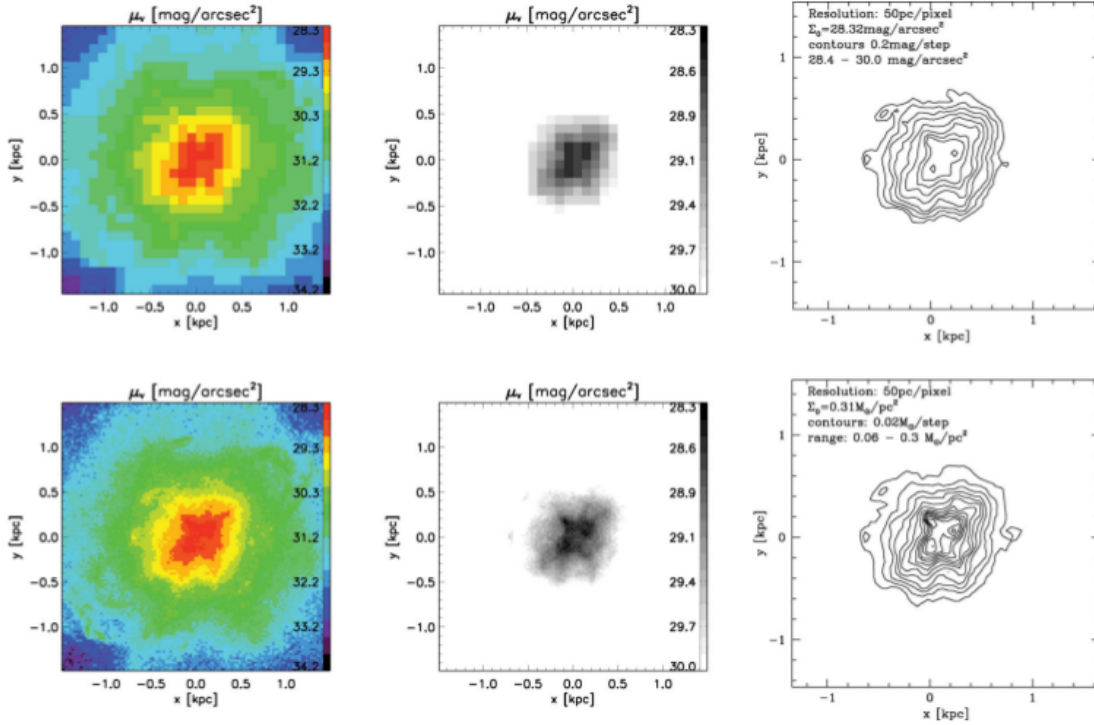


FIGURE 1.4: In the left and middle panel of both row we can see the two dimensional surface brightness maps with a resolution of 100 pc pixel$^{-1}$ (Top panels) and 25 pc pixel$^{-1}$ (Bottom panels). A cut of 30 mag arsec$^{-2}$ is apply in the middle panels. In the right panel are show the contour plots with a resolution of 50 pc pixel$^{-1}$, the upper row correspond a magnitude contours (logarithmic scale) and the bottom panel show a mass per pixel contour (linear scale). Credit to Assmann et al. (2013a)

Another major result from this model is the fact that even after 10 Gyr of evolution not all structures coming from the formation process are dissolved and survive inside the dSph galaxy. These remnants can affect the velocity dispersion because of coherent motions of stars stemming from the same SC.

Finally, they mention that even using an initial spherical distribution of the SCs they obtain a final object with ellipticities comparable with the classical dwarf galaxies. Also, they noticed that larger halo scalelenghts lead to higher ellipticities.

## 1.3 Dissolving star cluster scenario including angular momentum

Considering a hierarchical formation of the $\Lambda$ CDM model we said that dSph galaxies are considered to be the building blocks in galaxy formation, but in models like 1.2.1 and 1.2.2, to obtain these galaxies an interaction of other galaxies is needed, not using the dSph galaxy as building block. This is the main motivation of this thesis, use a dSph galaxy as seed to obtain a different one, a disc galaxy in this case.

In this project I want to expand the study of the dissolving star cluster model (Section 1.2.4) by introducing angular momentum into our distribution. In fact, our goal is to create a dSph galaxy in which the angular momentum is included from the start by giving all SCs the same sense of orbital direction in the x-y plane. Also, we reduce the z-component velocity of the SCs with the aim of form a more disc-like structure as the final luminous component and investigate if there is a defined transition region between final objects which are mainly pressure supported and dwarf disc galaxies, driven by rotation.
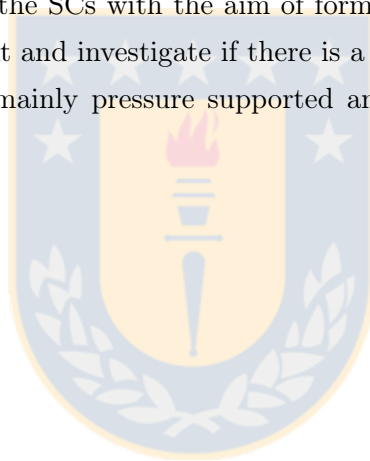
# Chapter 2

# The code: SUPERBOX

This chapter contains information about the code which was used to develop this thesis and I am going to describe some of the main characteristics of the code based on the information published by Fellhauer et al. (2000) and the code manual.

The code is called SUPERBOX and it uses the particle-mesh (PM) technique with moving high resolution sub-grids. The Fast Fourier Transform (FFT) utilization makes it very fast and suitable to work on desktop computers working even with millions of particles.

## 2.1 Particle-Mesh Technique

The PM technique covers the simulation area with a grid in which the particles are distributed. This density grid is then used to derive a grid of potential values by solving the Poisson equation. To do this, a transformation is applied to this density grid using a FFT algorithm in each time step and then, this is multiplied cell by cell with an suitable Green's function which is already transformed and is obtained by:

$$H_{i,j,k} = \frac{1}{\sqrt{i^2 + j^2 + k^2}} i, j, k = 0, 1, 2, ..., n$$

$$H_{0,0,0} = \frac{1}{\varepsilon} \tag{2.1}$$

From 2.1 it imply that the length of one cell is the unity and the cells number per dimension is $n$ which has to be power of two in order to use the FFT algorithm. $H_{0,0,0}$ is the force between particles in the same cell and was chosen $\varepsilon = 1$ to avoid problems such as "self acceleration".

To calculate the potential, the density grid is derived using the nearest grid point (NGP) scheme which assigns the mass of the particle to the nearest node. Now, the density grid is transformed by the utilization of a FFT algorithm:

$$\hat{\rho}_{a,b,c} = \sum_{i,j,k=0}^{n-1} \rho_{i,j,k} \cdot \exp\left(-\sqrt{-1}\frac{2\pi}{n}\left(a_i + b_j + c_k\right)\right) \qquad (2.2)$$

An already Fourier transformed Green's function (only once and at the beginning of the simulation) is multiplied cell by cell with the FFT-density grid. Then, this is back-transformed and the grid based potential is obtained:

$$\Phi_{i,j,k} = \frac{G}{n^3} \sum_{a,b,c=0}^{n-1} \hat{\rho}_{a,b,c} \cdot \hat{H}_{a,b,c} \cdot \exp\left(\sqrt{-q}\frac{2\pi}{n}\left(a_i + b_j + c_k\right)\right) \qquad (2.3)$$

## 2.2  Derivation of forces

The exerted force over a particle at a position $\bar{r}$ is given by

$$\overline{F}(\bar{r}) = -\overline{\nabla}\phi(\bar{r}) \qquad (2.4)$$

The accelerations are calculated using by numerical differentiation and the scheme that SUPERBOX uses is

$$a(x_i + dx) = \left.\frac{\partial \Phi}{\partial x}\right|_i + \left.\frac{\partial^2 \Phi}{\partial x^2}\right|_i \cdot \frac{dx}{\delta x} \qquad (2.5)$$

Where $a$ is the acceleration, $i$ es the i-th cell in the grid, $\delta x$ is the length of the cell and $dx$ is the deviation of the particle to the cell center.

Finally, the particle orbits are integrated using the leap-frog scheme:

$$v_{x,l}^{n+1/2} = v_{x,l}^{n-1/2} + a_{x,l}^{n} \cdot \Delta t$$

$$x_{l}^{x+1} = x_{l}^{n} + v_{x,l}^{n+1/2} \cdot \Delta t \tag{2.6}$$

A step by step summary of how SUPERBOX works is shown in Figure 2.1
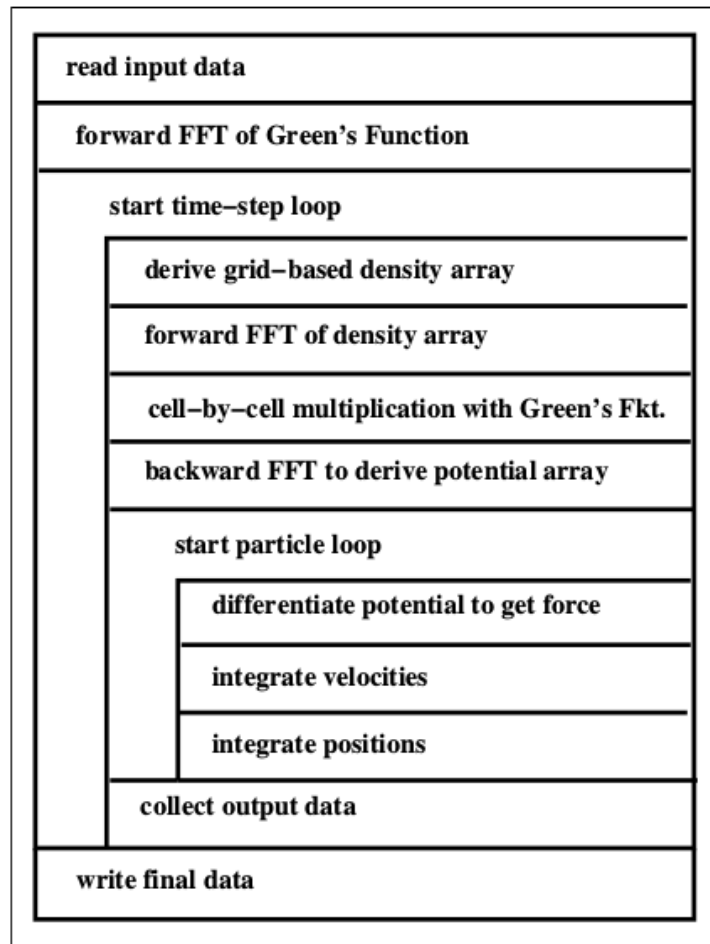


FIGURE 2.1: Step by step how SUPERBOX works. Credit to Fellhauer et al. (2000)

## 2.3   Grids

An important characteristic which distinguishes SUPERBOX from many other particle mesh codes is the multi-grid structure which can be implemented thanks to the linear additivity of potentials. The grids are used to focus and increase the resolution only in the place that it is necessary. This code has five different grids with three lengths which finally cover three different resolution levels as we can see in Figure 2.2.

The first grid has a length of $2 \times \text{R}_{core}$ and contains all the particles inside $\text{R}_{core}$ which are used to evaluate densities. This grid has the highest resolution and it is able to resolve the center of the object.

The length of the Grid 2 is $2 \times \text{R}_{out}$ and just as the previous grid all particles within $\text{R}_{core}$ are stored in it. The resolution of this grid is medium and can resolve the simulated object as a whole.

In the third grid we find all particles which are in the range $\text{R}_{core} < \text{r} \leq \text{R}_{out}$ and has the same resolution and size as the previous grid.

These first three grids are focused on a common center of the simulated object and move with it through the simulation area.

The Grid 4 has a length of $2 \times \text{R}_{system}$ which is equivalent to the entire simulation area. This grid just contain particles of the object with $\text{r} \leq \text{R}_{out}$ and it is a fixed grid with the lowest resolution.

The last grid is fixed as well and treats the particles that escape of the simulated object and stores those that are in $\text{r} > \text{R}_{out}$. Also, Grid 5 has the same resolution and size as Grid 4.

Using the PM technique an associated potential is calculated for each grid and then the total potential is obtained by the sum of individual potential from each grid:

$$\Phi(r) = [\theta(R_{core} - r) \cdot \Phi_1 + \theta(r - R_{core}) \cdot \Phi_2 + \Phi_3] \cdot \theta(R_{out} - r) + \theta(r - R_{out}) \cdot \Phi_4 + \Phi_5$$

$$\Phi(R_{core}) = \Phi_1 + \Phi_3 + \Phi_5$$

$$\Phi(R_{out}) = \Phi_2 + \Phi_3 + \Phi_5 \tag{2.7}$$

In these equations $\theta(\varepsilon) = 1$ for $\varepsilon > 0$ and $\theta(\varepsilon) = 0$ otherwise. As a result of equations 2.7 we know that for particles in the region $r \leq R_{core}$ the potential grids 1,3 and 5 are used. In the case that the particle is in $R_{core} \leq r \leq R_{out}$ the grids that are used are 2, 3 and 5. If the particle is in $R_{out} < r$ the grids used for the calculations are 4 and 5.

Finally, all particles that are in $R_{system} < r$ are no longer considered in the calculation and are removed.
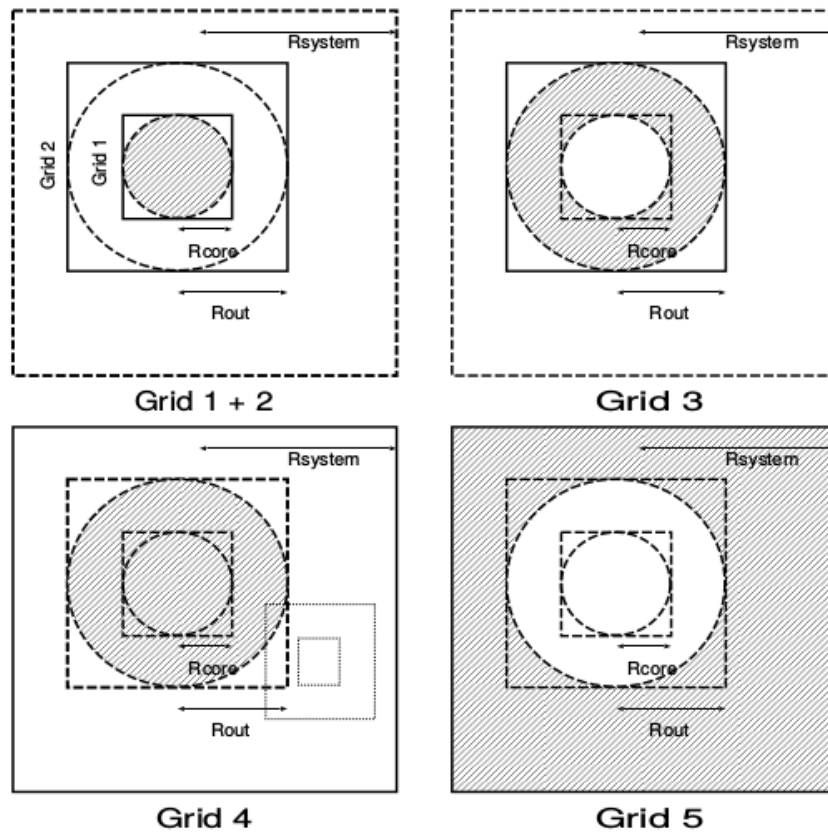


FIGURE 2.2: Superbox multi-grid structure. Each grid is separated using a solid line, the shadow represent the place of the grids where the particles are counted. Credit to Fellhauer et al. (2000)

# Chapter 3

# Setup

The dissolving star cluster model considers a DM halo and inside of it, the evolution of several SCs forming the luminous component of the dSph galaxy. To produce our DM halo we take in consideration that dSph galaxies could have cored DM haloes (Gilmore et al., 2007) so, in the simulations we use a Plummer sphere (Plummer, 1911) which is given by the equation:

$$\rho_{pl}(r) = \left( \frac{3M_{pl}}{4\pi R_{pl}^3} \right) \left( 1 + \frac{r^2}{R_{pl}^2} \right)^{\frac{5}{2}} \tag{3.1}$$

In Table 3.1 we detail the information that will be used to create the Plummer sphere which will represent our DM-halo. First, for this case we will use a million particles, a scale of length (radius of Plummer) of 1 kpc and a cut-off radius of 5 kpc and finally the total mass for this object will be $1.2 \times 10^8$ M$_\odot$, the enclosed mass is therefore $10^7$ M$_\odot$. We are following the Setup for the fidutial model of Assmann et al. (2013a) very closely.

| Characteristic | Value |
|---|---|
| Number of particles | $1,000,000$ |
| Plummer radius | 1 kpc |
| Cut-off radius | 5 kpc |
| Total mass | $1.2 \times 10^8$ M$_\odot$ |

TABLE 3.1: Initial values for our DM-halo. We model a Plummer sphere with a Plummer radius of 1 kpc using a 1000000 particles. The cut-off radius is chosen to be 5 kpc (=5 $R_{pl}$). The total mass of the halo is $1.2 \times 10^8$ M$_\odot$ which gives an enclosed mass within 500 pc of $10^7$ M$_\odot$. Table prepared by the author with the information to be used.

| Characteristic | Value |
| --- | --- |
| Number of particles | $100,000$ |
| Scale-length | $0.004$ kpc |
| Cut-off radius | $0.02$ kpc |
| SFE | $20\%$ |
| Initial mass | $7.5 \times 10^4$ M$_\odot$ |

TABLE 3.2: The Table shows the information to create a Plummer sphere that will represent a SC. For this case we use 100.000 particles with a scale-length of 0.004 kpc and a cut-off radius of 0.020 kpc. The sphere has an initial mass of $7.5 \times 10^4$ M$_\odot$ and a star formation efficiency (SFE) of 20 % . Table prepared by the author with the information to be used.

The luminous component of our final object is formed after the dissolution of several SCs and their evolution inside the DM halo. The number of SCs does not show significant differences in previous results of Assmann et al. (2013a,b) so, we consider an arbitrary initial number N = 30 SCs. For each one of the clusters we use a Plummer sphere (Eq. 3.1) modeled with $100,000$ particles following the recipe of Aarseth et al. (1974). The values of scale-length and cut-off are taken considering the observations of young SCs in the Antennae galaxy (Whitmore et al., 1999). Therefore, we take in our model 4 and 20 pc for Plummer and cut-off radius respectively. We know from Bressert et al. (2010) that the star formation rate (SFR) and star formation efficiency (SFE) is low in dSph galaxies so, in our case we used low mass open clusters with a SFE = 20%.

For simplicity all the SCs have the same mass and we know from (Alarcón Jara et al., 2018) that including star formation histories (SFH) does not change the results, so we will not consider them in this project and all our SCs are formed at the same time. Initially each SC has a mass of $7.5 \times 10^4$ M$_\odot$ which depends of the number of clusters (N) and SFE used. During our simulation a gas expulsion process is mimicked by reducing the mass of each particle in each cluster until a final total mass of the whole system of $4.5 \times 10^5$ M$_\odot$ after a crossing time of a SC (4 Myr) is reached. This final mass is typical for a classical dSph galaxy (eg. Mateo (1998)). Because we expect that most of the clusters are concentrated in the center, the SCs are distributed inside the DM halo following a Plummer sphere profile (Eq. 3.1). This sphere has a scale-length of 0.5 kpc and a cut-off radius of 2.5 kpc and the SCs are in virial equilibrium within the halo.

To summarize we have the tables 3.2 and 3.3. In this tables we detail all the necessary elements to form the SCs and the whole luminous component of the galaxy respectively. In the case of SCs we first require $100,000$ particles with a scale-lenght of 0.004 kpc and a cut-off radius of 0.020 kpc, where the SFE will be 20 % and the initial mass of each

| Characteristic | Value |
|---|---|
| Number of SCs | 30 |
| Scale-lenght | 0.5 kpc |
| Cut-off radius | 2.5 kpc |
| Final total mass | $4.5 \times 10^5$ M$_\odot$ |

TABLE 3.3: Information to create a Plummer sphere where the SCs will be distributed. For this we will use 30 SCs with a scale-length of 0.5 kpc and a cut-off radius of 2.5 kpc. The total mass of the whole system of SCs after the gas expulsion is $4.5 \times 10^5$M$_\odot$. Table prepared by the author with the information to be used.

of the clusters it will be $7.5 \times 10^4$ M$_\odot$. In the case of the luminous component, it will be formed using 30 clusters in a Plummer radius of 0.5 kpc and a cut-off radius of 2.5 kpc. Where the final mass will be equal to the sum of all the SCs after the gas expulsion process, that is, $4.5 \times 10^5$ M$_\odot$.

The initial positions of each SC in the system are given by a Plummer distribution and the initial orbital velocities are obtained by solving the Jeans equation:

$$\sigma_{r,i}^2 = \frac{1}{\rho_i(r)} \int_r^{rc} \frac{GM_{tot}(r')}{r'^2} \rho_i(r')dr' \tag{3.2}$$

In equation 3.2 $M_{tot}$ is the total mass which is the mass of all SCs and the DM halo mass.

In our study every cluster is orbiting the system in the same sense. To do that we use the angular momentum equation (Eq. 3.3) to verify it, if this is not the case and a cluster is orbiting in the other way we switch the sign of the velocities component $v_x$ and $v_y$. This procedure is available because the distribution function of a Plummer sphere (3.1) depends on the energy alone and does not depend on the angular momentum. With this, now our SCs are ready to start the simulations.

$$L_z = y \cdot v_x - x \cdot v_y \tag{3.3}$$

Now, we put all our objects together and run two different configurations with six simulations each one. Every simulation is run for 10 Gyr and a fixed time step of 0.2 Myr. The first configuration consist of a cored DM halo and 30 SCs which are spread following a Plummer distribution. Using as a base the initial distribution we create five models which are the initial one but the z-velocity component is now reduced to 90%, 75%, 50%, 0.25% and 10% of its initial value respectively. Then, in our second configuration we use the z-velocities from configuration 1 but force all SCs to start from a position with z$\equiv$

0. We run for this project 12 simulations in total.

In Table 3.4 we see the structure of this project will consists of two main parts, configurations 1 and 2. Each one of them will be developed using a cored DM-halo and 30 Plummer distributed SCs. During the development of both configurations, six simulations will be run in each one of them, which will represent a decrease in the z-velocity component of the original simulation. The decreases will be 90%, 75%, 50%, 25% and finally 10%. Each of the simulations runs for 10 Gyr, using a time-step of 0.2 Myr.

| Configuration 1 | Configuration 2 |
|---|---|
| Cored DM halo | Cored DM halo |
| 30 Plummer distributed SCs | 30 Plummer distributed SCs |
| no restriction | SCs are in z= 0 |
| $v_z$ reduction to 90%, 75%, 50%, 0.25% and 10% | $v_z$ reduction to 90%, 75%, 50%, 0.25% and 10% |
| simulations for 10 Gyr | simulations for 10 Gyr |
| Time-step of 0.2 Myr | Time-step of 0.2 Myr |

TABLE 3.4: Project structure, which is divided into two configurations formed by a cored DM-halo and 30 SCs. Each configuration also has six simulations where a velocity reduction in the z component of 90, 75, 50, 25 and 10 percent is applied. In configuration 2 we additionally force all SCs to start from z≡0. Each simulation runs for 10 Gyr using a time-step of 0.2 Myr. Table prepared by the author.

# Chapter 4

# Results

This project tries to investigate dwarf spheroidal galaxies which have angular momentum. Thus, we are performing simulations with two different initial conditions. The first set of models consist of regular Plummer-spheres in which all constituents have the same sense of motion in the x-y plane; is to say, a non-zero angular momentum in the z-direction. Within this set of models we reduce artificially the z-velocity to 90, 75, 50, 25 and 10% of its equilibrium value (first configuration). The second set of models places all constituents is to say, the SCs, artificially at z = 0 (second only). For each set of parameters we run 3 different random realizations. In this chapter we present the results of our simulations.

## 4.1 First Configuration

### 4.1.1 Velocity Space

In this section we will concentrate on analyzing the velocities of the final objects, both dispersion and rotation. The following figures (Figure 4.1 & 4.2) show two panels each, the upper panels in both cases are the velocity measurements in x-y plane and the lower ones x-z plane, also each panel has inside the evolution of corresponding velocity to radius of each $v_z$ reduction. This is for compare the behavior of the particles of the objects in both planes after the z-velocity reductions.

In our project we analyze the line of sight dispersion velocity by looking the profile that we obtain from the average of the three models in the $v_z$ reductions simulations which are shown in Figure 4.1. Each line with their respective color and figure represents one $v_z$ reduction (same for both panels). Blue pentagons re for 10% simulation, cyan up
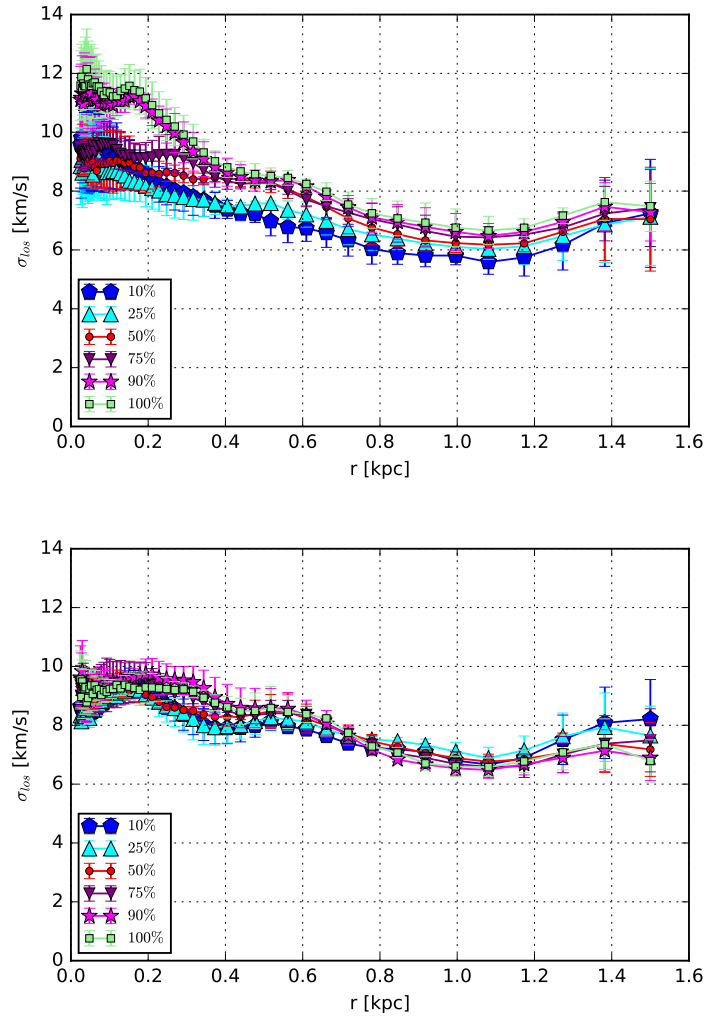
FIGURE 4.1: Line of sight velocity dispersion profiles obtained by the average of models 1, 2 and 3 in planes x-y (upper) and x-z (bottom). Blue pentagons are used for 10%, cyan up triangles for 25%, red circles for 50%, purple down triangles for 75%, magenta stars for 90% and finally light green squares for 100%. From this we note that our objects have characteristics of a dSph galaxy because the velocities are in the range of them (6-12 km/s) and follow a flat profile. The simulations are very close between them however, in the central region we note a decrease of velocity (x-y plane) meanwhile we reduce $v_z$. Image from this project.

triangles for 25%, red circles for 50%, purple down triangles for 75%, magenta stars for 90% and finally light green squares for 100%). From these dispersion profiles we can say that the final objects are consistent with a dSph galaxy because, they are in their range showing velocities between 6 to 12 km/s approx. (see Table 1.1) and also they follow a more or less flat profile. In the x-y plane we can see a small decrease in the central area of the objects after the reductions of $v_z$. On the other hand, although the velocity in the z component was reduced, the x-z plane does not shows any significant change between the simulations, but yes, the velocities in this plane are smaller than in x-y.
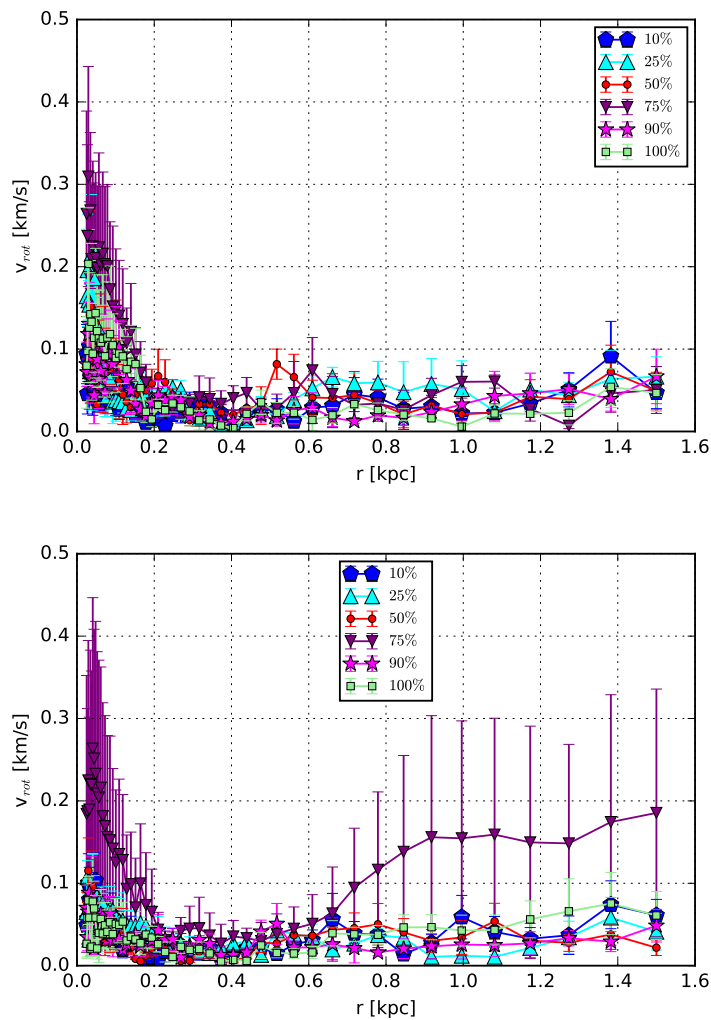
FIGURE 4.2: Rotation profiles of the six simulations of first configuration. In the upper panel is the profile from x-y plane and in the lower one x-y plane. The blue pentagons represent the object obtained after reducing the velocity $v_z$ to 10%, the cyan up triangles to 25%, red circles are used for the reduction to 50%, purple down triangles for 75%, magenta stars for 90% and finally light green squares for the initial simulation or 100%. In this case, we do not notice a clear tendency which relate the changes in velocity with the reductions of $v_z$ which follow a more or less flat profile having its higher values always in the central zone. Image from this project.

In Figure 4.2 we see the rotation velocity profiles for each reduction of $v_z$ where each line with their color and figure represent the average of the models of the configuration 1. The first thing that comes to mind when we look at the plots is that the rotation values are low and despite this, the highest value is always in the central area of our objects. Then, after 0.4 kpc the curves tends to be a more or less flat distribution. And finally we do not notice any trend that indicates a pattern that depends on the decreases of $v_z$.

In order to see what velocity dominates the final objects, we focus our attention of Figures 4.1 and 4.2 which represent the dispersion and rotational velocities respectively. In

the first case, we have velocities in a range of 6 - 12 km/s and in the second one an approximately range of 0 - 0.4 km/s. The rotation, despite being present in our objects, contributes very little to them and tends to be more concentrated in the central zone of the objects, although in the outskirts we also see that these increase slightly. In other hand, the dispersion dominated almost in the same way in the whole object and in every object of our results, even after reduce the z-velocity component of the SCs which formed the initial simulations.

### 4.1.2 Surface Brightness distribution

Another parameter in which we will put our attention is the surface brightness, knowing that the dSph galaxies reach values between 22 and 27 mag/arcsec$^2$ in their central zone (see Table 1.1). Figure 4.7 shows the surface brightness profiles in the x-y (upper) and x-z (lower) planes and as in the case of the analysis in the velocity map, the curves that make up this figure represent each of the velocity reduction simulations where blue pentagons correspond to 10% reduction, cyan up triangles to 25%, red circles to 50%, purple down triangles represent 75%, magenta stars for 90% and finally light green squares for 100%. When we analyzing this figure we noticed that as the reductions increase the final objects tend to increase slightly their surface brightness in both panels but specially in the x-z plane in the first 0.6 kpc. After the limit of 0.6 kpc we see a similar behavior in all simulations.

### 4.1.3 Ellipticity

The ellipticity $\epsilon$ is an structural parameter which can help us to understand how flat is our final object. The equation 4.1 give us this value:

$$\epsilon = 1 - \frac{b}{a} \tag{4.1}$$

Where in eq. 4.1 a and b are the major and minor axis respectively of an ellipse.

In this project we use the ELLIPSE task from IRAF which gives the ellipticity value at different radius. In our case we measure this parameter at a radius of 0.5 kpc. In Figure 4.4 the plots represent the average of the three random realizations in x-y plane (upper panel) and in x-z plane (lower panel), where we can see that the ellipticities tend to decrease after $v_z$ reductions, obtaining finally more spherical objects. Our values of
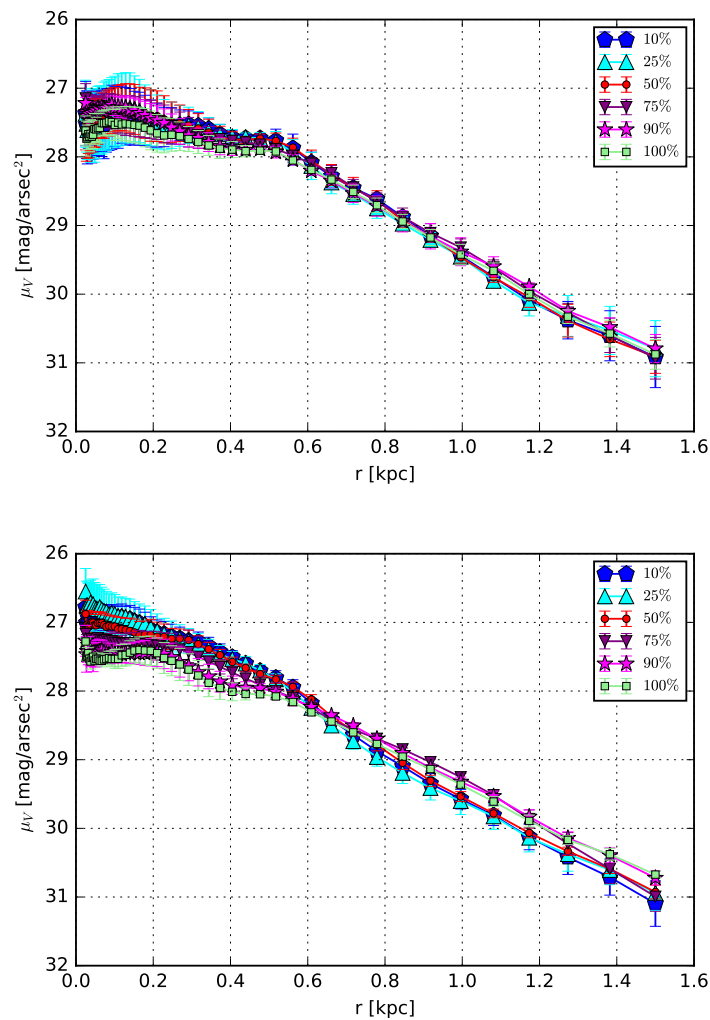
FIGURE 4.3: Surface brightness profiles of each reduction (averaged of the three models). Each color and its figure represent the reductions of $v_z$ where the blue pentagons are for 10% reduction, cyan up triangles to 25%, red circles to 50%, purple down triangles for 75%, magenta stars for 90% and finally light green squares for 100%. We see that the central surface brightness increases as $v_z$ is reduced. Image from this project.

ellipticity are in agreement with some dSph galaxies from the LG (McConnachie, 2012) or even they are higher.

## 4.2 Second Configuration

### 4.2.1 Velocity Space

In order to understand how the particles that make up the final objects are behaving, we have analyzed the dispersion velocities of each one of our results. Figure 4.5 shows
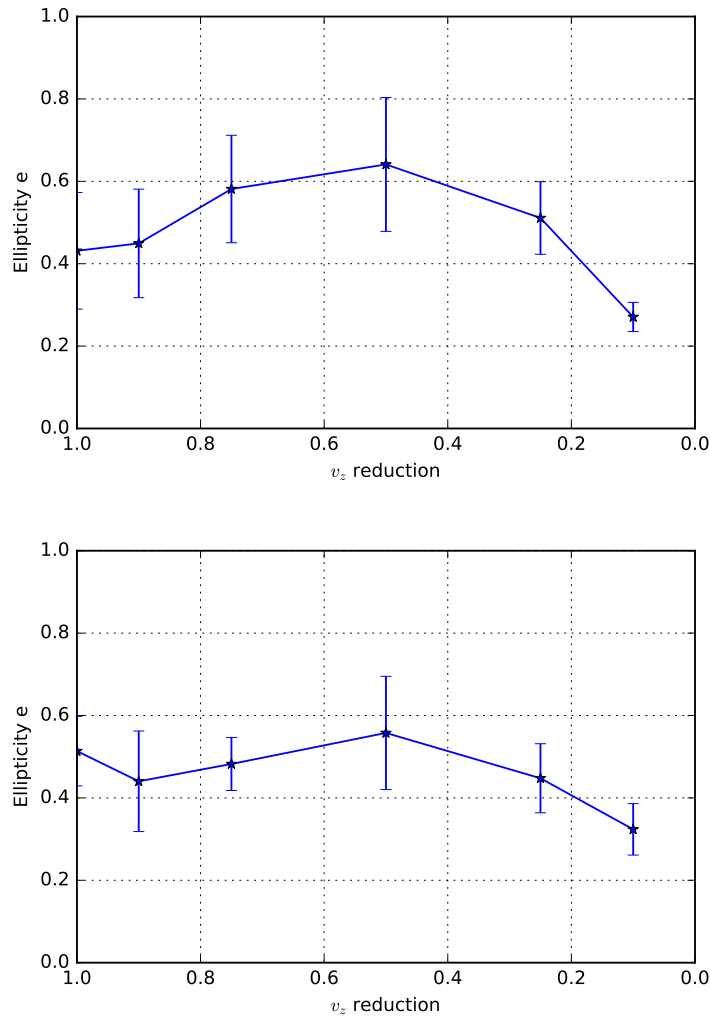
FIGURE 4.4: Values of ellipticity from the three different random realizations of configuration 1. On x-axis we have the $v_z$ reduction simulations and in y-axis the ellipticity obtained at 0.5 kpc by using ELLIPSE on IRAF with their respectively error. The upper panel shows the ellipticity variations in x-y plane and the lower one x-z plane. From this, we can say that our object tends to be more spherical meanwhile we reduce the z-velocity component. Image from this project.

the dispersion profiles of each simulation that form the configuration 2, where the curves represent the average of the three random models of the velocity reductions $v_z$. The upper panel shows the x-y plane dispersion velocities and from this we can observe that as we reduce $v_z$ the dispersion profile reach lower values, starting in the center from 12 km/s (100% simulation) until 6 km/s (10% simulation) approximately. From the lower panel we note that the dispersions do not vary so markedly after reductions. In both cases their values are in range that characterizes the dSph galaxies (see Table 1.1) and like their, our objects follow a more or less flat curve.

Now, if we check the rotational velocities to know if our objects are dominated by rotation

FIGURE 4.5: Dispersion velocity profiles of each simulation (average of the three models) of the second configuration. Upper panel is for x-y plane and lower for x-z. The colors and their respective figure represent the $v_z$ reduction simulations where blue pentagons are for 10% simulation, cyan up triangles for 25%, red circles for 50%, purpl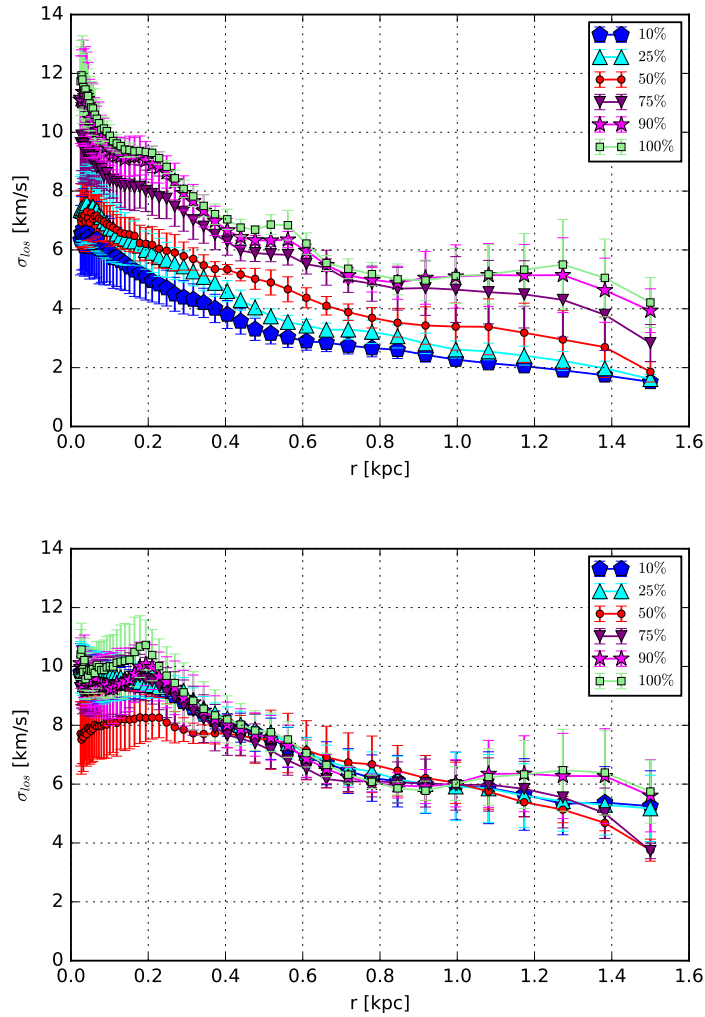e down triangles for 75%, magenta stars for 90% and light green squares for our initial simulation (100%). In this comparative plot we can see that the dispersion profiles are very similar between them in the x-z plane despite the $v_z$ reduction, however in the x-y we see a reduction as $v_z$ decrease. Both cases show a more or less flat profile and are in the range of velocities of the dSph galaxies. Image of this project.

or dispersion we see Figure 4.6 which shows the rotation profiles for all the $v_z$ reductions, where the colors and figures are the same that in the whole project (blue pentagons are for 10% simulation, cyan up triangles for 25%, red circles for 50%, purple down triangles for 75%, magenta stars for 90% and light green squares for 100%). In x-y plane (upper panel) we see a little contribution of rotation in the center of the objects reaching their highest values in the two first simulations (100 and 90%) Also, in the x-z plane we can not see a significant contribution and as the previous case the higher velocities are concentrated in the center of the objects. In both cases we can not see a clearly trend which indicate a relation between $v_z$ reductions and rotation velocities.
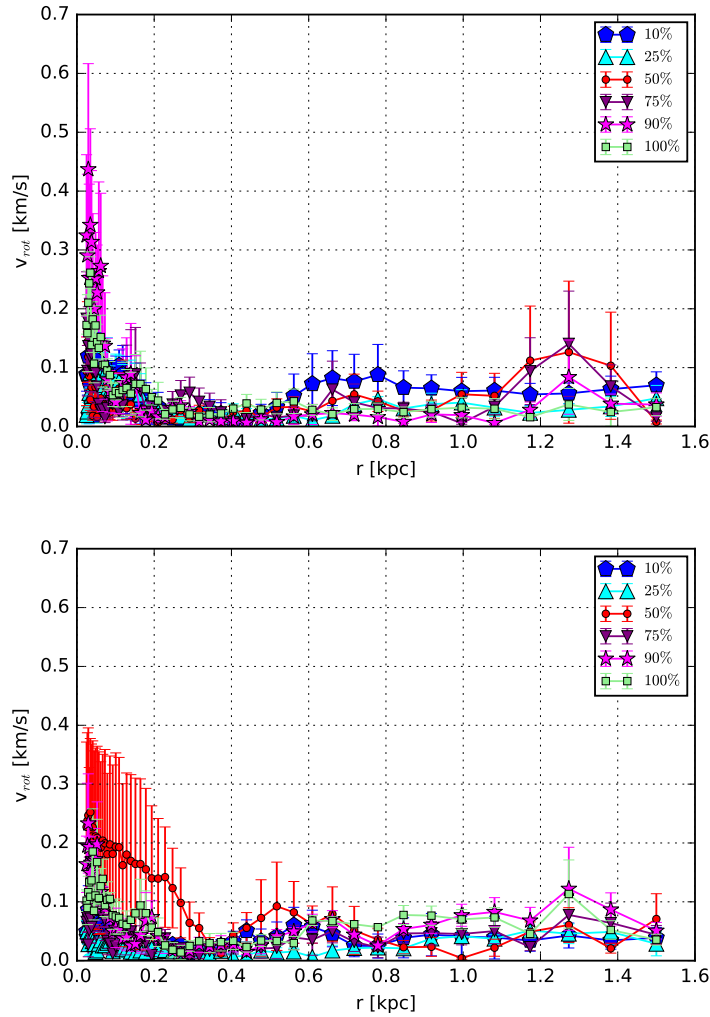
FIGURE 4.6: Rotational velocity profiles of the six final objects of configuration 2. Upper panel is for x-y plane and lower for x-z, the colors and figures represent each $v_z$ reduction where blue pentagons are for 10% simulation, cyan up triangles for 25%, red circles for 50%, purple down triangles for 75%, magenta stars for 90% and light green squares for our initial simulation (100%). Here we can not see a clearly trend which indicates changes in the velocities however, the highest values of each plane always is reached in the central zone. Image from this project.

Considering figures 4.5 and 4.6 and with the aim to understand which velocity dominates our objects we find with their that in this configuration that dispersions are greater and dominate in all the points of the final objects. Despite to have rotational velocities in all our results these are no so significant reaching values below 1 km/s.

### 4.2.2 Surface Brightness distribution

In Figure 4.7 we show the surface brightness profiles of the resultant objects of each z-velocity reduction simulation in both x-y and x-z planes (upper and lower panels respectively), where the average of the corresponding velocity reduction of the three models

of configuration 2 is represent by blue pentagons for 10% simulation, cyan up triangles for 25%, red circles for 50%, purple down triangles for 75%, magenta stars for 90% and light green squares for 100%. In the x-y panel we do not see a difference in the reductions but in the x-z plane we see an increase of surface brightness inside of 0.2 kpc as we increase the $v_z$ reductions.

With respect to the outer parts of the final objects we can notice that as we decrease the z-velocity of the SCs, the outer part becomes fainter in x-z plane. Explicitly in our initial simulation we have an approximate surface brightness for the farthest point of 31 mag/arcsec$^2$ and then we have 32 mag/arcsec$^2$ from the reduction to 75% keeping in the following reductions. In the initial simulation and in the first two reductions of $v_z$ the brightest point of the final object is not necessarily in the center, but it is in the central zone. Finding ourselves with this, may be the product of some remains of the evolution of the SCs. On the other hand, from the last three reductions we find that the brightest point is in the center and then decreases linearly as the radius increases. Finally, if we compare this with the central surface brightness of dSph galaxies (see Table 1.1) we can note that our objects are in agreement with a them.

### 4.2.3  Ellipticity

To know about the shape of our final objects is that we help ourselves with the ELLIPSE task of IRAF (see 4.1.3) which we use to measure the ellipticity at 0.5 kpc. Figure 4.8 shows in x-y (upper panel) and x-z (lower panel) plane how the ellipticity of each resulting object changes as the z-velocity is reduced. According to this figure we note that while the velocity $v_z$ decreases the ellipticity decrease on the x-y plane and increase in x-z, this mean that we can find a disk like structure after the reductions.
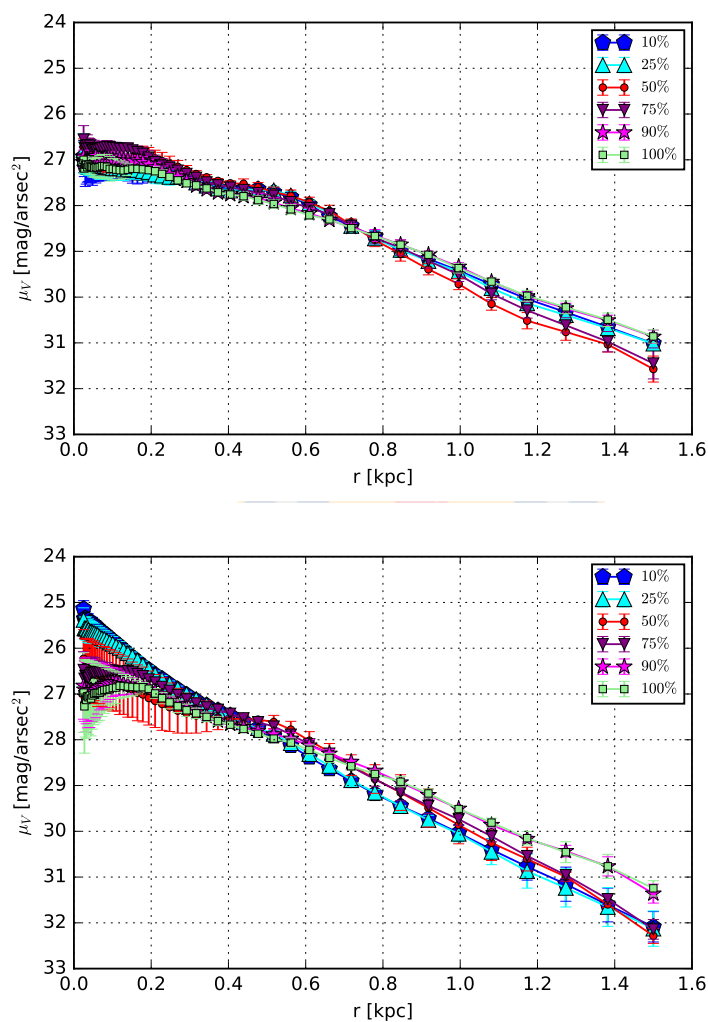
FIGURE 4.7: Surface brightness profile of our final objects. The upper panel is for x-y plane and the lower for x-z. Blue pentagons represent to 10% v$_z$ reduction simulation, cyan up triangles for 25%, red circles for 50%, purple down triangles for 75%, magenta stars for 90% and light green squares for 100%. Here we can see an central surface brightness increase while we reduce v$_z$ in x-z plane. Image from this project.

FIGURE 4.8: Values of ellipticity from the average of the three different random realizations of configuration 2. On the x-axis we have the $v_z$ reduction simulations and in the y-axis the ellipticity obtained at a radius of 0.5 kpc. Here we find an ellipticity decrease in the x-y plane and and increase in x-z plane which is an indicate of a possible disk-like structure in our objects. Image from this project.

# Chapter 5

# Discussion and Conclusions

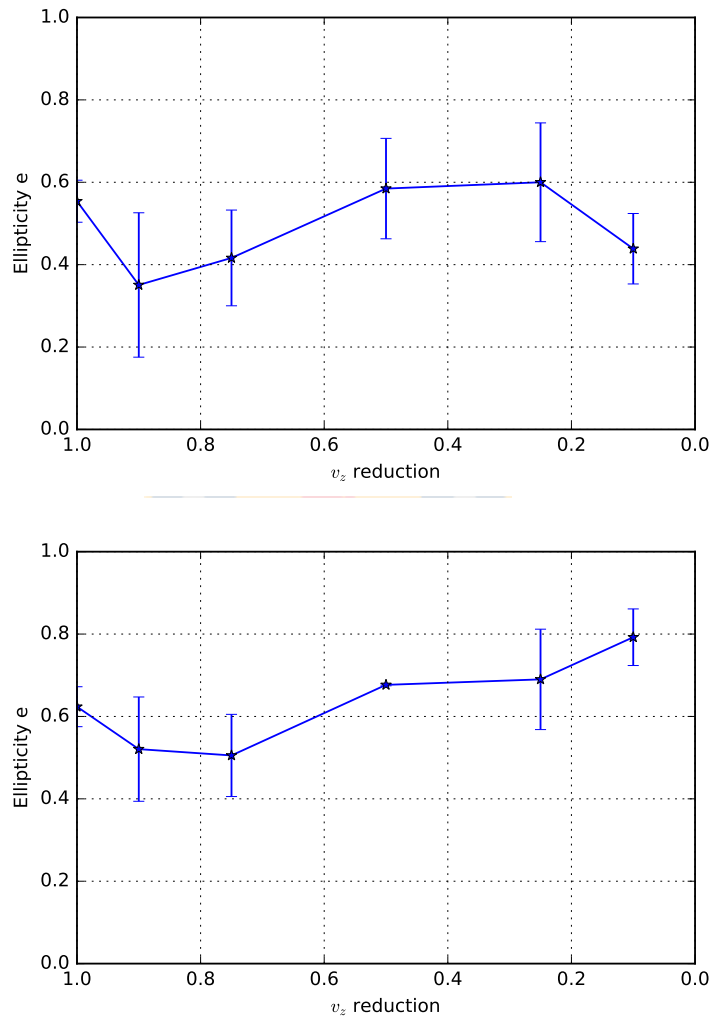After reviewing the results obtained in our project it is necessary to check the most important results. If we analyze each configuration separately we note that in the first configuration we find objects that are very similar which share characteristics with dSph galaxies.

When we analyzed the ellipticities at 0.5 kpc we realized that they tend to become smaller and therefore we finally have more spherical objects, contradicting our expectations.

If we take our attention in the velocity space we find that all our objects are strongly dominated by the dispersion with velocities between 6 and 12 km/s which do not show many differences when comparing the simulations with different $v_z$. However, after the reductions made, a slight decrease in the dispersion was observed mainly in the central areas of the objects (x-y plane). Also, each one of our objects follow a flat profile leading to think that here we are in presence of dSph galaxies. In this configuration we see rotations in a range of 0 - 0.4 km/s approx which tend to reach their maximum values in the central areas of the objects or the external zones where it acquires a rise but less noticeable than that observed in the center. Unfortunately, when we analyzed the rotations we can not see a clear pattern that indicates a connection between the reductions of $v_z$ and the behavior of the rotation profiles.

Finally, we look at what happens with the surface brightness of the objects. This parameter shows some differences as the velocity $v_z$ is reduced. We noticed that the central surface brightness increases gradually with each reduction reaching to have close to a

point of difference between the initial simulation and the final two of them in x-z plane.

During the review of the second configuration which differs from the first one because we limit the positions of the SCs to z = 0 we find that in this case even though our objects also share characteristics with the dSph galaxies they also show some improvements that lead us to our goal.

In terms of dispersion velocities we note that all our reductions behave similar in x-z plane, however in x-y we see a decrease as $v_z$ reduction is increase. In this configuration we also find profiles more or less flat in both planes and with velocities in agreement with dSph galaxies. The rotation does not follow an ordered profile, however in general we see that it becomes more present in the central area. The rotation values are low compared to the dispersion since in all the simulations we find velocities lower than 0.5 km/s which confirms that the dispersion dominates in each one of the final objects.

Looking at the surface brightness profiles we see that in the x-y plane there are no major changes and all the objects behave in a similar way, however, in the x-z plane we see an increase in the central surface brightness as the reductions of v $_z$ increase.

Finally, when we look at the ellipticities we find that our objects tends to be more spherical in x-y plane and flatter in x-z plane leading to think that we are in presence of a possible disk-like structure in the second configuration.

Now, if we compare both configurations it is possible to say that in both cases we have objects dominated by dispersion in range of dSph galaxies even following flat profiles. Despite to have rotational velocities this do not reach a significant value. In other hand the surface brightness do not show a important change while we reduce $v_z$ despite to have a little increase in both configurations. Finally, the shape of the objects of configuration 1 tends to be more spherical in both planes but in the second configuration we could obtain a possible disk-like structure after a reduction of $v_z$ at 50%.

With this project we could obtain disk-like structures (second configuration) from a dSph galaxies including angular momentum but these also are objects which are dominated by dispersion velocities and not for rotational as we hoped.

# Bibliography

Aarseth S. J., Henon M., Wielen R., 1974, A&A, 37, 183

Abdo A. A., et al., 2010, Astrophysical Journal, 712, 147

Alarcón Jara A. G., Fellhauer M., Matus Carrillo D. R., Assmann P., Urrutia Zapata F., Hazeldine J., Aravena C. A., 2018, Monthly Notices of the Royal Astronomical Society, 473, 5015

Assmann P., Fellhauer M., Wilkinson M. I., Smith R., 2013a, Monthly Notices of the Royal Astronomical Society, 432, 274

Assmann P., Fellhauer M., Wilkinson M. I., Smith R., Blaña M., 2013b, Monthly Notices of the Royal Astronomical Society, 435, 2391

Battaglia G., Helmi A., Breddels M., 2013, Nature, 57, 52

Bressert E., et al., 2010, Monthly Notices of the Royal Astronomical Society: Letters, 409, L54

D'Onghia E., Besla G., Cox T. J., Hernquist L., 2009, Nature, 460, 605

Fellhauer M., Kroupa P., Baumgardt H., Bien R., Boily C., Spurzem R., Wassmer N., 2000, New Astronomy, 5, 305

Feng J. L., 2010, Annual Review of Astronomy and Astrophysics, 48, 495

Gilmore G., Wilkinson M., Kleyna J., Koch A., Evans W., Wyse R., Grebel E., 2007, Nuclear Physics B - Proceedings Supplements, 173, 15

Grebel E. K., III J. S. G., Harbeck D., 2003, The Astronomical Journal, 125, 1926

Kauffmann G., White S. D. M., Guiderdoni B., 1993, Monthly Notices of the Royal Astronomical Society, 264, 201

Klypin A., Kravtsov A. V., Valenzuela O., Prada F., 1999, The Astrophysical Journal, 522, 82

Lada C. J., Lada E. A., 2003, Annual Review of Astronomy and Astrophysics, 41, 57

Lokas E. L., 2011, Acta Physica polonica B,

Majewski S. R., et al., 2005, The Astronomical Journal, 130, 2677

Mateo M., 1998, Annual Review of Astronomy and Astrophysics, 36, 435

Mayer L., Kazantzidis S., Mastropietro C., Wadsley J., 2007, Nature, 445, 738

McConnachie A. W., 2012, The Astronomical Journal, 144, 4

Planck Collaboration et al., 2016, A&A, 594, A13

Plummer H. C., 1911, Monthly Notices of the Royal Astronomical Society, 71, 460

Porter T. A., Johnson R. P., Graham P. W., 2011, Annual Review of Astronomy and Astrophysics, 49, 155

Sawala T., Scannapieco C., Maio U., White S., 2010, Monthly Notices of the Royal Astronomical Society, 402, 1599

Walker M. G., Mateo M., Olszewski E. W., Gnedin O. Y., Wang X., Sen B., Woodroofe M., 2007, The Astrophysical Journal Letters, 667, L53

White S. D. M., Rees M. J., 1978, Monthly Notices of the Royal Astronomical Society, 183, 341

Whitmore B. C., Zhang Q., Leitherer C., Fall S. M., Schweizer F., Miller B. W., 1999, The Astronomical Journal, 118, 1551

York D. G., et al., 2000, The Astronomical Journal, 120, 1579